Pressure induced band inversion, electronic and structural phase transitions in InTe: A combined experimental and theoretical study

V. Rajaji,[1,2] Koushik Pal,[1,2] Saurav Ch. Sarma,[3,2] B. Joseph,[4] Sebastian C. Peter,[3,2]
Umesh V. Waghmare,[5,2] and Chandrabhas Narayana[1,2,*]

[1]*Chemistry and Physics of Materials Unit, Jawaharlal Nehru Centre for Advanced Scientific Research, Jakkur, Bangalore 560 064, India*
[2]*School of Advance Materials, Jawaharlal Nehru Centre for Advanced Scientific Research, Bangalore 560 064, India*
[3]*New Chemistry Unit, Jawaharlal Nehru Centre for Advanced Scientific Research, Jakkur, Bangalore 560 064, India*
[4]*Elettra Sincrotrone Trieste, S.S. 14, Km 163.5 in Area Science Park, Basovizza, Trieste 34149, Italy*
[5]*Theoretical Sciences Unit, Jawaharlal Nehru Centre for Advanced Scientific Research, Bangalore 560 064, India*

(Received 5 November 2017; revised manuscript received 16 April 2018; published 27 April 2018)

We report high-pressure Raman scattering measurements on the tetragonal phase of InTe corroborated with the first-principles density functional theory and synchrotron x-ray diffraction measurements. Anomalous pressure-dependent linewidths of the A_{1g} and E_g phonon modes provide evidence of an isostructural electronic transition at ∼3.6 GPa. The first-principles theoretical analysis reveals that it is associated with a semiconductor-to-metal transition due to increased density of states near the Fermi level. Further, this pressure induced metallization acts as a precursor for structural phase transition to a face centered cubic phase ($Fm\bar{3}m$) at ∼6.0 GPa. Interestingly, theoretical results reveal a pressure induced band inversion at the Z and M points of the Brillouin zone corresponding to pressures ∼1.0 and ∼1.4 GPa, respectively. As the parity of bands undergoing inversions is the same, the topology of the electronic state remains unchanged, and hence InTe retains its trivial band topology ($\mathbb{Z}_2 = 0$). The pressure dependent behavior of the A_{1g} and E_g modes can be understood based on the results from the synchrotron x-ray diffraction, which shows anisotropic compressibility of the lattice in the a and c directions. Our Raman measurements up to ∼19 GPa further confirms the pressure induced structural phase transition from a face-centered to primitive cubic ($Fm\bar{3}m$ to $Pm\bar{3}m$) at $P \sim 15$ GPa.

DOI: 10.1103/PhysRevB.97.155158

I. INTRODUCTION

Pressure is a powerful tool to alter the interatomic bond distances, forces, density, electronic structure, and, consequently, material intrinsic characteristics. Pressure effects on an anisotropic crystal structure (i.e., anisotropic bonding exists in different crystallographic directions) have received increasing attention in recent years due to their abilities to induce the exotic electronic and topological changes in materials with strong spin-orbit coupling (SOC) [1–4]. For example, a typical transition-metal dichalcogenide (TMD) with formula MX_2 (M = transition metal and X = S, Se, and Te) compounds shows strong covalent bonding in the ab directions (in plane) and weak van der Waals bonding along the c direction (out of plane) [2,3]. As a consequence of structural anisotropy, the properties of the TMD materials also show anisotropy. For instance, the $NbSe_2$ compound shows an anisotropic transport property under pressure [5]. Some TMD systems such as $MoSe_2$ and MoS_2 show large structural anisotropy during hydrostatic compression, leading to a semiconductor-to-metal transition at high pressure [2,3]. Binary layered chalcogenide based strong SOC compounds A_2B_3 (A = Bi, Sb and B = Se, Te, S) exhibit electronic topological transition (ETT) at high pressure [6–10]. Theory predicts that InSb, InSe, monolayer of TlS, and TlSe compounds are pressure induced topological insulators (TIs) [11–13]. The above illustrated examples show the importance of pressure effects on the anisotropic and strong SOC materials for tuning the various interesting properties in it. Motivated by these observations, we have investigated the possibility of pressure induced electronic and topological phase transitions in the binary layered semiconductor InTe, which is a TlSe prototype with strong SOC.

The topological quantum phase transition (TQPT) is a nonadiabatic process in which the topological invariant quantity $\mathbb{Z}_2$ changes from 0 to 1, as a consequence of continuous tuning of the SOC strength [14]. The band inversion at the time-reversal invariant momenta (TRIM) points of the Brillouin zone and parity exchange (odd/even) between the valence-band maximum (VBM) and conduction-band minimum (CBM) are the necessary conditions for the TQPT [12,14,15]. For example, pressure induced nontrivial TQPT has been theoretically predicted in many systems and experimentally observed in BiTeI, Sb_2Se_3, BiTeBr, and 1T-$TiTe_2$ compounds [4,6,16,17]. The typical experimental signatures of the TQPT can be obtained from Raman linewidths of the sample through the electron-phonon coupling mechanism [4,6,18]. Band inversion in the electronic structure of the material often gives rise to increased density of states (DOS) in the valence and conduction bands, and subsequent increase in electrical conductivity, Seebeck coefficient, and hence the enhancement of thermoelectric performance of the material [19].

Indium telluride (InTe) and other III-VI layered semiconductors have received extensive attention due to their

*Corresponding author: cbhas@jncasr.ac.in

potential application for photovoltaic and photoconducting devices [20,21]. InTe crystallizes in the TlSe-type structure [$B37$, space group (SG) $I4/mcm$, $Z = 8$] at ambient conditions with mixed valent formula $In^{1+}In^{3+}Te_2^{2-}$. The trivalent indium In^{3+} ions are tetrahedrally coordinated by four Te^{2-} ions, whereas monovalent In^{1+} ions are surrounded by eight Te^{2-} ions [22]. Recently, it was shown [23] that in InTe, the lone pairs of $5s^2$ electrons of the In^{1+} act as rattlers, leading to intrinsic ultralow lattice thermal conductivity ($0.4\,Wm^{-1}\,K^{-1}$) through a strong anharmonic phonon-phonon interaction, giving a figure of merit (ZT) of 0.9 at 600 K. Some studies have been carried out in the aspect of high-pressure structural phase transitions in InTe [22,24–26]. A synchrotron x-ray diffraction (XRD) study has revealed that InTe undergoes a pressure induced structural transition from tetragonal ($B37$, SG: $I4/mcm$, $Z = 8$) to a face-centered-cubic phase ($B1$, SG: $Fm\bar{3}m$, $Z = 4$) at ∼6.1 GPa and then to a primitive cubic phase ($B2$, SG: $Pm\bar{3}m$, $Z = 1$) at 14 GPa [25]. The structural transition ($B37$ phase to $B1$ phase) is proceeded by a semiconductor-to-metal transition at ∼5 GPa due to the modification of In^{1+} and In^{3+} to In^{2+} [26]. Furthermore, the recent high-pressure transport measurement shows an unusual thermoelectric nature under pressure [25]. Raman spectroscopy is a sensitive local probe, which has been extensively used for studying the structural, electronic, and topological changes in materials [6–10,18,27,28]. Hence, it will be important to probe the pressure-dependent behavior of InTe using Raman scattering measurements and complement it with the first-principles theoretical calculations to gain insights into the systematics of the phase transitions and also reveal indications regarding any isostructural electronic transitions.

In this work, we have systematically investigated the pressure-dependent behavior of InTe through the Raman scattering measurements and the first-principles calculations on InTe along with the high-pressure XRD measurements up to ∼5.7 GPa. An isostructural electronic transition was observed from the unusual electron-phonon coupling of the Raman modes (A_{1g} and E_g) at ∼3.6 GPa which is associated with the metallization, evident from the calculated electronic structure of InTe. Interestingly, our calculations reveal pressure induced band inversions in InTe at an even number of points in the Brillouin zone near 1.0–1.4 GPa. Furthermore, the high-pressure Raman results provide signatures of pressure induced structural phase transitions ($B37 \rightarrow B1 \rightarrow B2$) in agreement with previous XRD studies [25].

II. EXPERIMENTAL DETAILS

Stoichiometric amounts of In powder (99.5%) and Te shot (99.99%) were mixed and sealed in evacuated quartz tubes, which were slowly heated to 700 °C within 8 h, held for 3 days and then cooled to room temperature in 10 h. Phase identity and purity of the sample were determined by powder XRD experiments, which were carried out using synchrotron radiation with the wavelength $\lambda = 0.4957$ Å, at the Xpress beam line of the Elettra Synchrotron, Trieste. The Rietveld refinement of the obtained powder XRD pattern of the sample confirms the pure tetragonal phase of InTe.

Raman spectroscopy measurements were conducted on a custom-built Raman spectrometer equipped with a four-level solid-state frequency-doubled Nd:YAG laser of wavelength $\lambda = 532$ nm, Horiba Jobin Yvon monochromator (550 mm focal length), and liquid-nitrogen-cooled CCD detector [29]. The spectral resolution was $\sim 1\,cm^{-1}$ for the grating of 1800 grooves per mm. The spectrometer was calibrated with the Si sample and Ne light source. The pressure was generated using a Mao-Bell-type diamond anvil cell (DAC) with culet diameter size of 400 μm. The stainless steel (T301) was used as a gasket and it was preindented to about 60 μm thickness. A hole of about 150 μm diameter was drilled at the center of the indentation, which acts as the sample chamber. The pressure was calculated using the Ruby fluorescence technique [30]. Ruby spheres of ∼5 to 10 μm were placed inside the gasket hole along with the InTe sample for the pressure measurements. A mixture of methanol-ethanol in the ratio of 4:1 was used as the pressure-transmitting medium (PTM), which ensures the hydrostatic conditions up to 10 GPa [31]. Typical accumulation time for each Raman spectrum was about 10 minutes for each pressure point.

The high-pressure powder XRD experiments were performed at the Xpress beam line of the Elettra Synchrotron, Trieste, Italy with a wavelength $\lambda = 0.4957$ Å using a Mao-Bell DAC. A MAR345 image plate detector was used to collect the diffraction pattern, and the obtained image [two-dimensional (2D)] format was converted to an intensity versus 2θ (1D) plot using the FIT2D software [32]. LaB_6 is used for initial diffraction setup adjustments and to determine an accurate sample to detector distance, which in the present case is 312.8 mm. The gasket preparation and the pressure determination method are the same as discussed above. Initially, the unit-cell parameters for pressure-dependent XRD patterns were determined using the POWD and DICVOL software [33,34]. Further, these values were verified by the Lebail fitting method using the FULLPROF software [35].

III. COMPUTATIONAL METHODS

First-principles density functional theoretical (DFT) calculations were carried out using the QUANTUM ESPRESSO [36] (QE) software, in which the potential energy arising from the interaction between the core electrons and the nucleus is replaced with a smooth pseudopotential [37]. To treat the exchange and correlation energy of electrons, we used a generalized gradient approximation (GGA) [38] with a functional form of the Perdew-Burke-Ernzherof flavor [39]. Expansion of wave functions and charge density in the plane-wave basis set was truncated with energy cutoffs of 60 and 240 Ry, respectively. Brillouin-zone integrations were sampled on an $8 \times 8 \times 8$ uniform mesh of k points, smearing the discontinuity in the occupation numbers of the electrons with the Fermi-Dirac distribution function with a width (k_BT) of 0.003 Ry. Effects of SOC were included in our calculations of the electronic structure through the use of fully relativistic pseudopotentials [40], while we used scalar-relativistic ultrasoft pseudopotentials in the calculations of phonons. In the simulation of pressure-dependent properties, we optimized the structure with respect to lattice constants and atomic coordinates to minimize the enthalpy, $H = E + PV$. We obtained lattice dynamical properties using DFT linear response (also known as density functional perturbation theory [41]) as

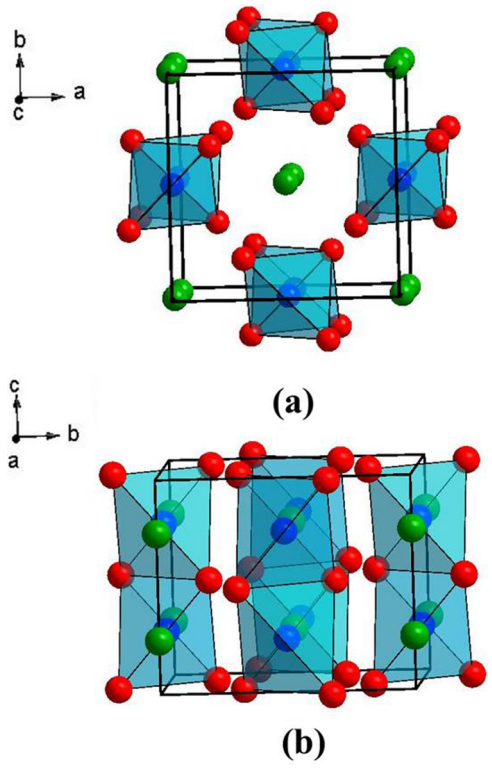

FIG. 1. The unit cell of InTe along the (a) *ab* projection and (b) *bc* projection. Here, the green, blue, and red color spheres represent the In^{1+}, In^{3+}, and Te^{2-} ions, respectively.

implemented in the QE distribution [36]. To assess the bulk electronic topology of InTe, we used Z2PACK code [42] to determine the $\mathbb{Z}_2$ topological invariants. This code uses hybrid Wannier functions [43,44] and employs the ideas of time-reversal polarization in the determination of the $\mathbb{Z}_2$ invariants.

IV. RESULTS

A. Raman scattering measurements

1. Tetragonal phase of InTe under pressure

InTe adopts a tetragonal structure (D_{4h}^{18}) at ambient conditions with $In^{3+}(1)$ and $In^{1+}(2)$ atoms occupying, respectively, 4*a* and 4*b* sites and Te^{2-} atoms occupying 8*h* sites. The layered structure of InTe is different from the usual TMD structure, as it adopts an $In^{1+}In^{3+}Te^{2-}$ configuration with one In^{3+} atom and four Te^{2-} atoms forming a tetrahedral with In^{3+} at the center [see Fig. 1(a)]. This covalently bonded In^{3+}-Te^{2-} tetrahedra is connected by common horizontal edges and forms a linear chain along the crystallographic *c* axis [see Fig. 1(b)] [22,23]. The In^{1+} atom is arranged in between the two tetrahedral layers via weak electrostatic force along the *a* and *b* axes.

As the primitive unit cell of InTe has eight atoms, according to the group theoretical analysis for the centrosymmetric tetragonal structure of the InTe shows 24 zone-center phonon modes at the Γ point:

$$\Gamma = A_{1g} + 2A_{2g} + B_{1g} + 2B_{2g} + 3E_g + B_{lu} + 3A_{2u} + 4E_u.$$

Here, the subscripts g and u represent Raman-active *gerade* and IR-active *ungerade* modes, respectively. There are 12

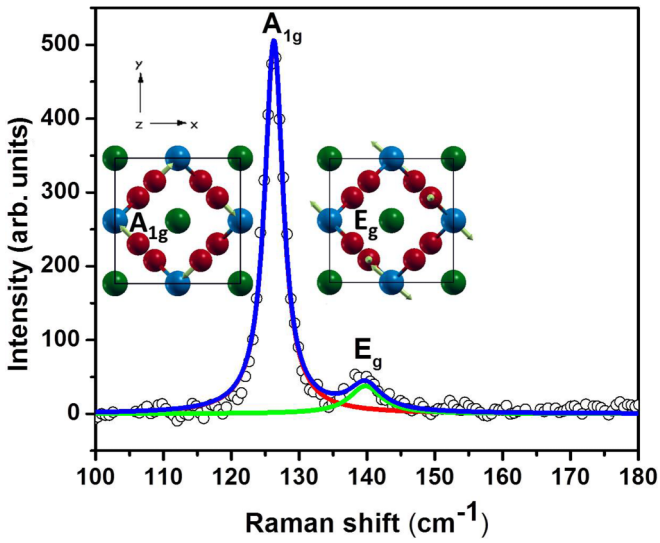

FIG. 2. Raman spectrum of InTe at ambient conditions. Visualization of the atomic displacement patterns for the A_{1g} and E_g modes are given in the inset. For the A_{1g} mode, only Te (red) atoms move in the *xy* plane as indicated by the arrows, whereas for the E_g mode, In^{3+} (blue) and Te (red) atoms vibrate along the *xy* plane and *z* direction, respectively. In both of these modes, the In^{1+} (green) atoms sitting in the hollow cage of the crystal structure do not exhibit any displacement.

Raman-active modes ($A_{1g} + 2A_{2g} + B_{1g} + 2B_{2g} + 3E_g$) and nine IR-active modes ($B_{lu} + 2A_{2u} + 3E_u$). Even though 12 Raman optical modes are theoretically predicted, experimentally we could see only two modes above 100 cm^{-1} (see Fig. 2). An earlier polarization-dependent Raman study on InTe single crystals by Nizametdinova identified the phonon symmetries of the observed modes as E_g (46 cm^{-1}, 139 cm^{-1}), A_{1g} (126 cm^{-1}), and B_{1g} (86 cm^{-1}) [45]. Our Raman spectrum (above 100 cm^{-1}) matches well with this report. Based on the work of Nizametdinova [45], the observed phonon modes at ∼126 and ∼139 cm^{-1} are assigned to A_{1g} and E_g symmetry, respectively. We would like to further mention that our phonon assignment matches well with the previously reported ambient Raman studies of InTe by Torres *et al.* [20]. The customized Raman setup used for the present high-pressure study can detect the signal only from 100 cm^{-1} due to the specific edge filter [29], thus limiting the observation of low-frequency modes [E_g (46 cm^{-1}) and B_{1g} (86 cm^{-1})] [45]. Further, the possible reason for the detection of the lower number of Raman modes than the predicted ones could be due to their lower scattering cross sections. The experimental detection is limited by the signal-to-noise (S/N) ratio of the spectrometer used, and hence it is practically impossible to detect modes with lower scattering cross sections. Detecting a lower number of Raman active modes than expected is commonly observed in Raman spectroscopy [9,10,27]. Atomic displacement patterns for the A_{1g} and E_g modes are shown in the inset of Fig. 2. The Lorentzian function was used to fit the Raman modes and extracted frequencies, linewidths, and intensities.

Lattice dynamical properties are known to play an important role in the electronic or topological transitions of a material [4,6–10,28,46]. Hence to understand the pressure-dependent electronic and topological properties of InTe, it is very

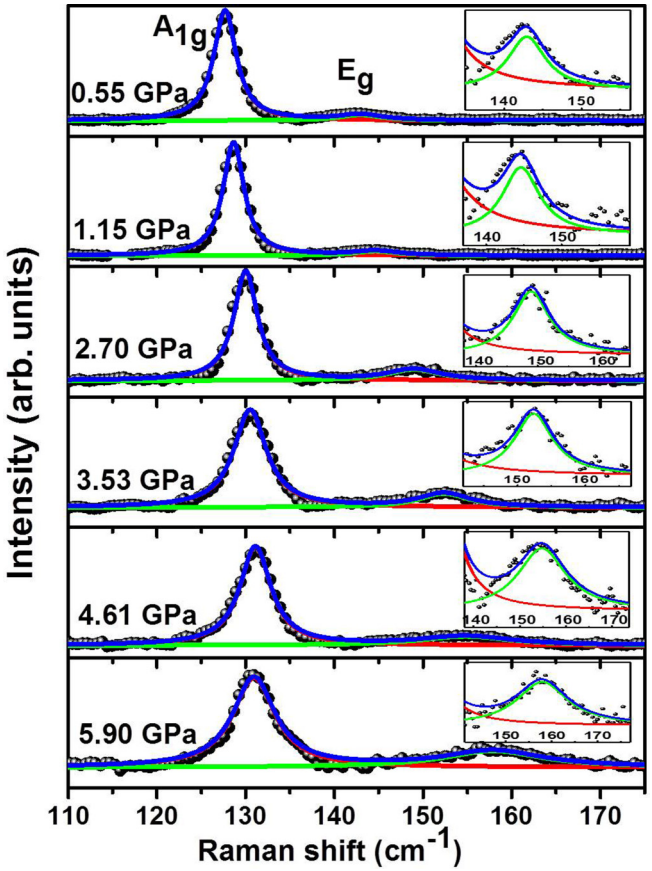

FIG. 3. Pressure evolutions of Raman spectrum of InTe (tetragonal phase) at selected pressure values (below 6 GPa). The inset shows the zoomed-in view of the E_g mode fitting for the sake of clarity. The red, green, and blue color curves represent the fitting of the A_{1g} mode, E_g mode, and cumulative peak, respectively.

essential to study the behavior of the phonon modes of the $B37$ phase. First, we present a detailed analysis of phonons as a function of pressure for the tetragonal phase of InTe. Figure 3 represents the pressure evolution of InTe up to ∼6.0 GPa. The pressure dependence of the phonon frequencies for A_{1g} and E_g modes is as shown in Figs. 4(a) and 4(b). The phonon mode frequencies A_{1g} and E_g are monotonically increasing up to ∼6.0 GPa with a small change in the slope at ∼3.6 GPa. The nonlinear pressure dependence of the A_{1g} mode is analyzed by the quadratic equation for two different pressure regions (0–6.0 and 0–3.6 GPa), and the details are presented in the Supplemental Material [47]. The pressure-dependence behavior of the E_g mode is fitted using a linear equation, whereas the A_{1g} mode is fitted by second order (from ambient to ∼3.6 GPa) and linear equation between ∼3.6 and ∼6.0 GPa [7–9]. Table I shows the pressure coefficients and Gruneisen parameter, and it can be observed that pressure coefficient (a_1) of the A_{1g} mode (2.3 cm^{-1} GPa^{-1}) is smaller than the E_g mode (3.9 cm^{-1} GPa^{-1}). Recall that the intralayer consists of a covalently bonded Te^{2-}-In^{3+}-Te^{2-}-In^{3+} chain of atoms, whereas the interlayers are separated by means of weak electrostatic interactions [23,24] between the negatively charged $In^{3+}Te_4^{2-}$ tetrahedra and In^{1+} atom. Hence, it is natural to expect that the pressure coefficient of the E_g mode will be greater than the A_{1g} mode, which is consistent with our experimental observation.

In Raman spectroscopy, the full width at half maximum (FWHM) is inversely proportional to the phonon lifetime in a crystalline system, and hence the Raman linewidth analysis provides valuable information about the isostructural electronic transition [6–10,27,48]. Figures 4(c) and 4(d) shows the experimental pressure-dependent linewidth behavior of the A_{1g} and E_g phonon modes. The linewidth of both modes (A_{1g} and E_g) shows hardly any changes up to 3.6 GPa, but above this pressure, there is a sudden increase. Generally, the spectral linewidth (or FWHM) will increase with respect to the applied hydrostatic pressure. But here the observed anomalies in their linewidth at ∼3.6 GPa are unusual and indicate that the origin is due to electron-phonon coupling. The linewidth behavior of both modes (A_{1g} and E_g) is almost similar and suggests that phonon modes interact strongly with the electronic states which are being modulated by pressure beyond ∼3.6 GPa. The intensity of the A_{1g} and E_g modes is monotonically decreased under pressure with a sudden change in its slope at ∼3.6 GPa [Figs. 4(e) and 4(f)]. The observed Raman results are reproducible in multiple runs. Since InTe undergoes a first-order structural transition only at ∼6 GPa [25], the observed anomaly in our experiment cannot be due to a structural transition. Thus, the observed phonon anomalies (frequencies, linewidths, and intensities) at ∼3.6 GPa clearly suggest an isostructural electronic transition.

2. Structural phase transitions in InTe under pressure

To explore the Raman signatures of the pressure induced structural transitions in InTe, a high-pressure Raman scattering experiment was carried out up to ∼18.7 GPa, the maximum pressure reached in this study. Figures 5(a) and 5(b) represent the pressure evolution of the Raman spectrum and the pressure-dependent Raman frequencies of InTe up to ∼18.7 GPa, respectively. Upon increasing pressure, two major changes are noticed at ∼6 and ∼15 GPa. The disappearance of the E_g mode and the discontinuity of the A_{1g} mode [Fig. 5(b)] at ∼6 GPa indicates the structural transition from tetragonal ($B37$) to sixfold-coordinated NaCl-type cubic phase ($B1$, SG: $Fm\bar{3}m$, $Z = 4$) [24,25]. Though the transition occurs near ∼6 GPa, the very small intensity of the A_{1g} peak was still observed in 6–7.5 GPa, which suggests the coexistence of the $B37$ phase in the $B1$ cubic phase region. This happens commonly when it is a displacive pressure induced phase transition. Recently, more accurate synchrotron XRD results by Jacobsen *et al.* showed a pressure induced structural transition from NaCl type to eightfold-coordinated CsCl type ($B2$, SG: $Pm\bar{3}m$, $Z = 1$) at around 14 GPa [25]. Since factor group analysis for cubic phases of InTe ($B1$ and $B2$) predicts no Raman-active modes, it is expected to be impossible to identify the transition point for the NaCl- to CsCl-type structural transition using Raman spectroscopy. However, upon increasing pressure, at ∼15 GPa, a new mode starts to appear at ∼153 cm^{-1}, which is in the $B2$ phase region, as suggested by the XRD measurements [25]. Our observations suggest that broader linewidth of this new peak may be due to a defect induced mode in the $B2$-type phase, which has been observed in binary semiconductors [49]. There is another possible reason for the observation of

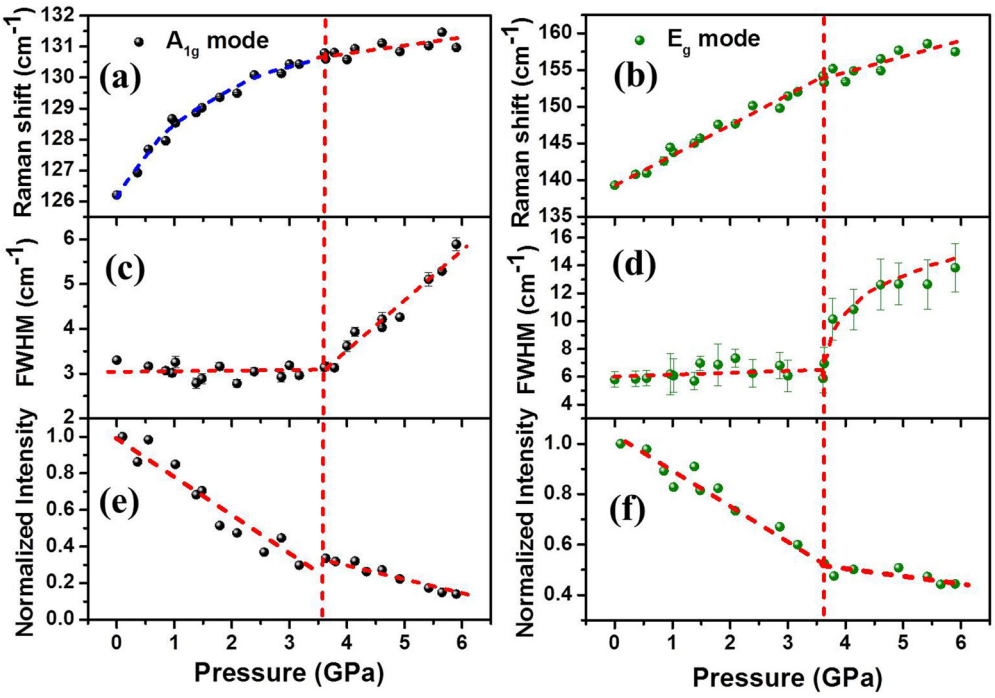

FIG. 4. Pressure dependence of Raman shift of (a) A_{1g} and (b) E_g modes. FWHM of (c) A_{1g} and (d) E_g modes. The normalized intensity of (e) A_{1g} and (f) E_g modes. The red dotted lines in (a) and (b) represent the linear equation fit, whereas the blue dotted line in (a) represents the second-order (quadratic) equation fit. The red dotted lines in (c)–(f) represent a guide to an eye. The vertical dotted line at ∼3.6 GPa represents the isostructural electronic transition in InTe.

broad peaks in Raman spectra of cubic structures, namely, the appearance of the second-order Raman spectra [50]. We observe that the pressure induced structural transition sequences ($B37 \rightarrow B1 \rightarrow B2$) from Raman scattering agree well with results obtained by previous XRD reports and are reversible [22,24,25].

B. Synchrotron XRD measurements

Earlier XRD studies of the InTe compound under pressure established the structural phase transitions ($B37 \rightarrow B1 \rightarrow B2$) in this system [22,24,25]. However, there was less attention paid to the pressure dependence of the lattice parameters at the low-pressure regime. In order to shed light on the isostructural transition as well as the anisotropic compressibility of the a and c axes of the tetragonal phase ($B37$) of InTe, we have undertaken systematic high-pressure synchrotron XRD measurements up to ∼5.7 GPa only. The ambient XRD pattern (outside DAC) is recorded from a rotating capillary tube (filled with InTe powder sample) method. The obtained ambient 2D image is converted into a 1D pattern using FIT2D software. The Rietveld refinement of the synchrotron XRD pattern at ambient condition is shown in Fig. 6. The calculated unit-cell parameters are $a = b = 8.4589$ Å, $c = 7.1578$ Å, and volume $V = 512.17$ Å^3, and the atomic fractional coordinates of $In^{3+}(1)$, $In^{1+}(2)$, and $Te^{2-}(3)$ are (0, 0, 0.25), (0, 0.5, 0.25), and (0.181, 0.681, 0), respectively, which agree well with the literature [51]. The fitting parameters associated with Fig. 6 are $R_p = 7.13$, $R_{wp} = 8.00$, and chi-square (χ^2) = 0.721. The synchrotron XRD patterns of the polycrystalline InTe sample show tetragonal phase stability up to ∼5.7 GPa, which is in good agreement with our Raman results and recent XRD work [25]. Due to the presence of the texture effect in the obtained XRD patterns, we could not do the full Rietveld refinement. However, we have analyzed the synchrotron XRD patterns for

TABLE I. Experimental Raman-mode frequencies and pressure coefficients of the A_{1g} and E_g modes at both room pressure and ∼3.6 GPa as obtained from fits to the data using $\omega(P) = \omega(P_0) + a_1(P - P_0) + a_2(P - P_0)^2$ and $\omega(P) = \omega(P_0) + a_1(P - P_0)$, respectively. The Gruneisen parameters γ are calculated by using the relation $\gamma = (\frac{B}{\omega(P0)} \times \frac{\partial\omega}{\partial P})$, where B represents the isothermal bulk modulus ($B = 20.60$ GPa).

Raman mode	Pressure regions (GPa)	Mode frequency $\omega(P_0)$ (cm^{-1})	a_1 (cm^{-1} GPa^{-1})	a_2 (cm^{-1} GPa^{-2})	γ
A_{1g}	0–3.6	126.3 ± 0.1[a]	2.3 ± 0.2[a]	-0.3 ± 0.0[a]	0.38
A_{1g}	3.6–6.0	130.2 ± 0.3[b]	0.2 ± 0.0[b]		0.03
E_g	0–3.6	139.7 ± 0.3[a]	3.9 ± 0.2[a]		0.58
E_g	3.6–6.0	145.9 ± 2.0[b]	2.1 ± 0.5[b]		0.30

[a]Estimated at ambient pressure ($P_0 = 1$ atm).
[b]Estimated at $P_0 = 3.6$ GPa.

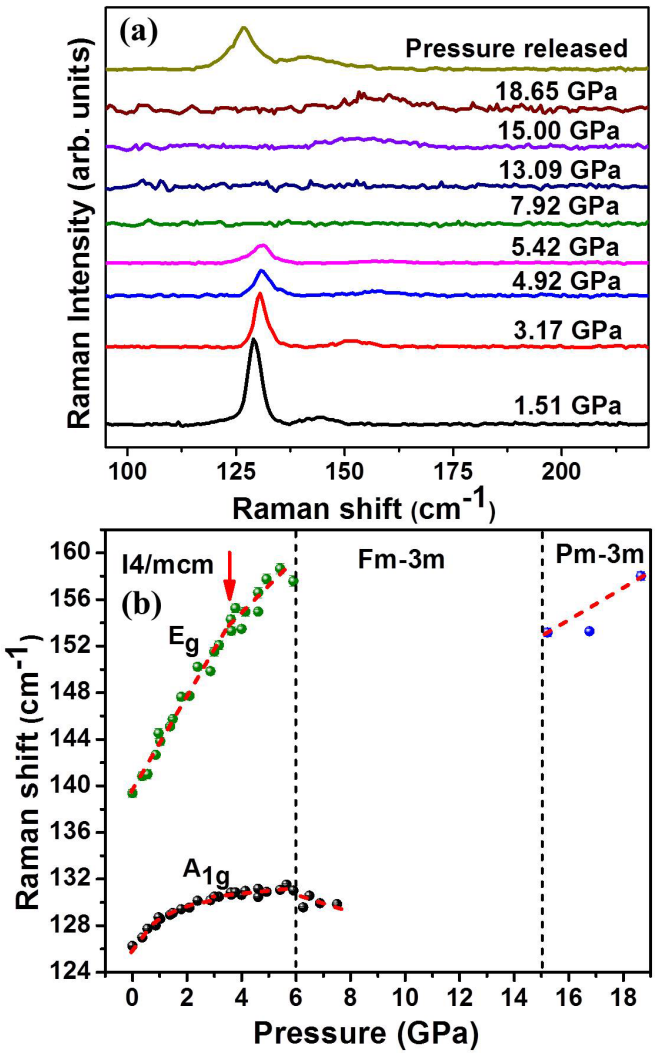

FIG. 5. (a) Pressure evolution of Raman spectrum of InTe at selected pressure values and (b) pressure vs Raman shift of InTe up to ∼18.65 GPa. The vertical dotted lines at ∼6 and ∼15 GPa represent the structural transition from $B37$ to $B1$ type and $B1$ to $B2$ type, respectively. The red dotted line represents a guide to the eye. The solid red arrow at ∼3.6 GPa indicates the isostructural electronic transition.

each pressure value by the Le Bail refinement method using FULLPROF software [35]. The representative Le Bail fit of the synchrotron patterns at $P = 1.41$ and $P = 3.94$ GPa is shown in Figs. 7(a) and 7(b), respectively (for other pressure values, please see Figs. S2(a) and S2(b) in the Supplemental Material [47]). The Le Bail refinement method can give the accurate unit-cell parameters (a, b, c, and V) within the permitted error bar and their associated fitting parameters are not truly significant. Hence, we did not mention the fitting parameters in Figs. 7(a) and 7(b).

The pressure dependence of the comparison between the experimental and theoretical lattice parameters (a and c) of InTe is shown in Figs. 8(a) and 8(b). Figure 8(d) represents the pressure versus relative unit-cell dimensions (a/a_0, c/c_0) and V/V_0 ratio. Also, Fig. 8(d) clearly illustrates the anisotropic compressibility along the a and c axes. The pressure vs a and c of the experimental data is fitted by the third-order Birch

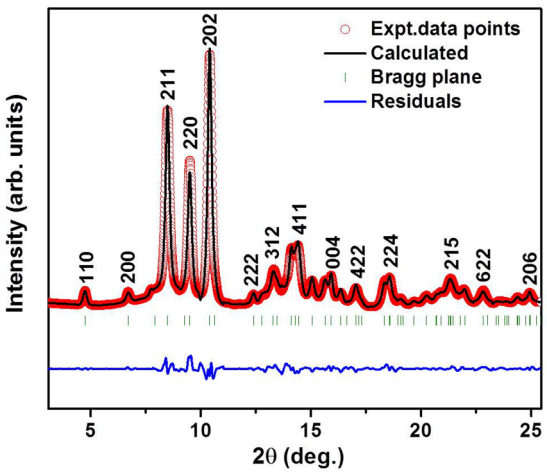

FIG. 6. Rietveld refinement of synchrotron XRD pattern of InTe at ambient conditions (outside DAC). The wavelength of synchrotron XRD used in the experiment is $\lambda = 0.4957$ Å.

Murnaghan equation of state (BM EOS) [52] using EOSFIT7 software [see Figs. 8(a) and 8(b)]. The fit yields the linear compressibility of lattice parameter a, $K_a = K_b = 19.19 \times 10^{-3}$ GPa^{-1}, and that of b, $K_c = 10.08 \times 10^{-3}$ GPa^{-1}. Hence, the c axis is stiffer than the a axis, which is consistent with our Raman spectroscopic results and, quantitatively, the a axis (and b axis) is about 1.9 times more compressible than the c axis. Also, the c/a ratio increases monotonically with pressure, as shown in the inset of Fig. 8(b). Further, Chattopadhyay *et al.* [22] have shown a decreasing c/a ratio (c axis is more

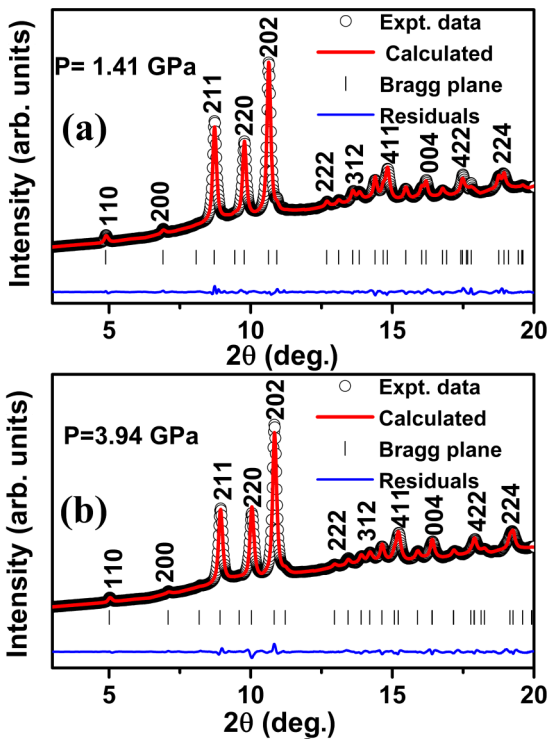

FIG. 7. (a) Le Bail fit to the synchrotron XRD patterns of InTe at ∼1.41 GPa (b) 3.94 GPa. The wavelength $\lambda = 0.4957$ Å was used for the pressure-dependent synchrotron XRD measurements.

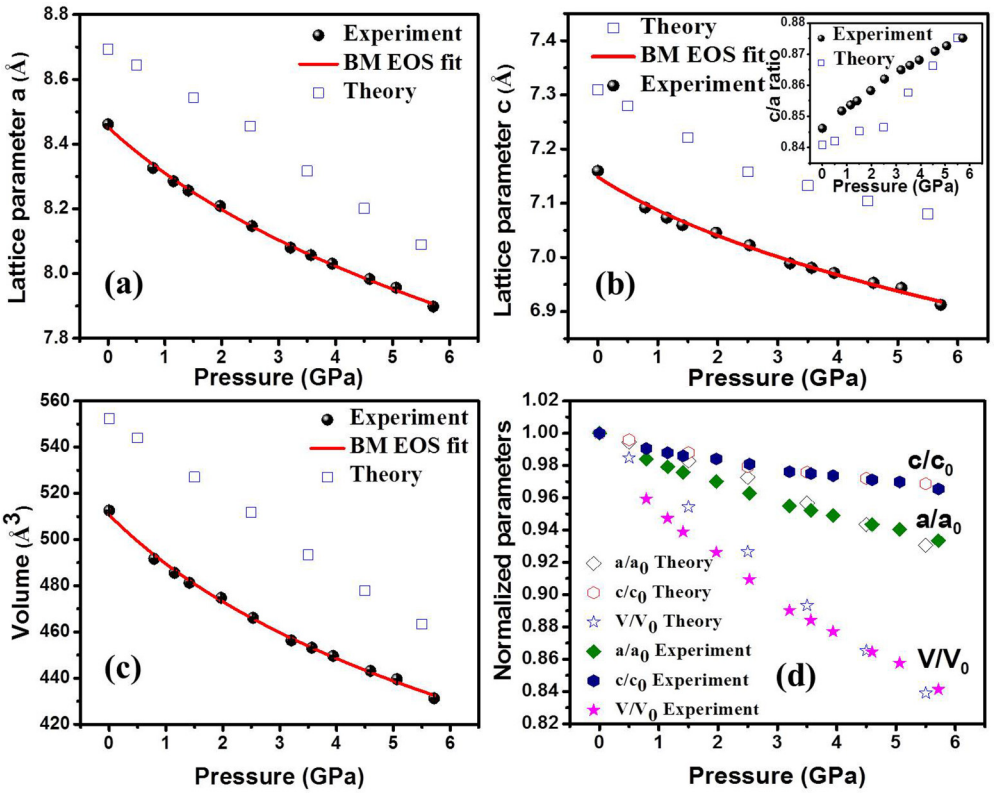

FIG. 8. Experimental and DFT calculated lattice parameters (a) a, (b) c, (c) V, and (d) relative unit-cell parameters (a/a_0, c/c_0, and V/V_0) as a function of applied hydrostatic pressure. Here, a_0, c_0, and V_0 are the values of lattice constants (a and c) and volume at 0 GPa. The inset of (b) shows the pressure vs c/a ratio. The red solid line represents the third-order Birch-Murnaghan equation-of-state fit for the tetragonal phase of InTe.

compressible than a axis) in the tetragonal phase of InTe under pressure (see Fig. S3 in the Supplemental Material [47]), which is counterintuitive with respect to bonding present in the crystal structure and is in contradiction with our results. We like to emphasize here that the axial compressibility (c/a ratio) is directly linked to the specific bonding (along a, b, and c axes) in the crystal structure and our results of anisotropic compressibility [a (or b) and c axes] and Raman pressure coefficients of the A_{1g} and E_g modes are consistent with each other and are in line with that expected from the crystal structure bonding in InTe. It is noteworthy that cell parameters a, c, and the c/a ratio do not show any anomalies within the experimental resolution. The experimental pressure-dependent volume is fitted by third-order BM EOS using the equation given below and is shown in Fig. 8(c) [52],

$$P(V) = \frac{3B_0}{2}\left[\left(\frac{V_0}{V}\right)^{\frac{7}{3}} - \left(\frac{V_0}{V}\right)^{\frac{5}{3}}\right] \times \left\{1 + \frac{3}{4}(B_0' - 4)\left[\left(\frac{V_0}{V}\right)^{\frac{2}{3}} - 1\right]\right\},$$

where V_0, B_0, and B_0' represent the volume at room pressure, the isothermal bulk modulus, and its derivative, respectively. The fit yields $B_0 = 20.60$ GPa, $V_0 = 510.69$ Å^3, and derivative of bulk modulus $B_0' = 6.24$, and the obtained values match well with the earlier report [25].

C. Theoretical calculations

To understand the observed isostructural anomaly at ~3.6 GPa, first-principles calculations were carried out for the tetragonal phase ($B37$) of InTe as a function of pressure. Our estimates of the optimized lattice constants of InTe are $a = 8.69$ Å and $c = 7.30$ Å, which are overestimated compared to their experimental values [51] ($a = 8.45$ Å and $c = 7.15$ Å), as is typical of GGA-DFT calculations. Variation in the calculated lattice constants (a and c) with pressure [shown in Figs. 8(a) and 8(b)] agrees with our experiments. The calculated lattice constants are slightly overestimated (~2.7% for a and ~2% for c) with respect to their experimental values, but are within the typical errors of DFT calculations using the GGA exchange-correlation functional. As a result of the overestimation of the a and c lattice constants, the calculated volume [Fig. 8(c)] of the unit cell is also overestimated (by ~7%). More importantly, the calculated pressure dependence of the relative unit-cell parameters a/a_0, c/c_0, and V/V_0 [Fig. 8(d)] agrees remarkably well with their experimental counterparts. Here, a_0, c_0, and V_0 are the lattice constants and volume at 0 GPa. These results suggest that our DFT calculations are in good agreement with experiment.

The calculated c/a ratio [see inset of Fig. 8(b)] increases with pressure, also in overall agreement with the experimentally measured c/a ratio. Notably, the small deviation in the c/a ratio trend is observed between the experiment (like convex shape) and theoretical (like concave shape) values [see inset

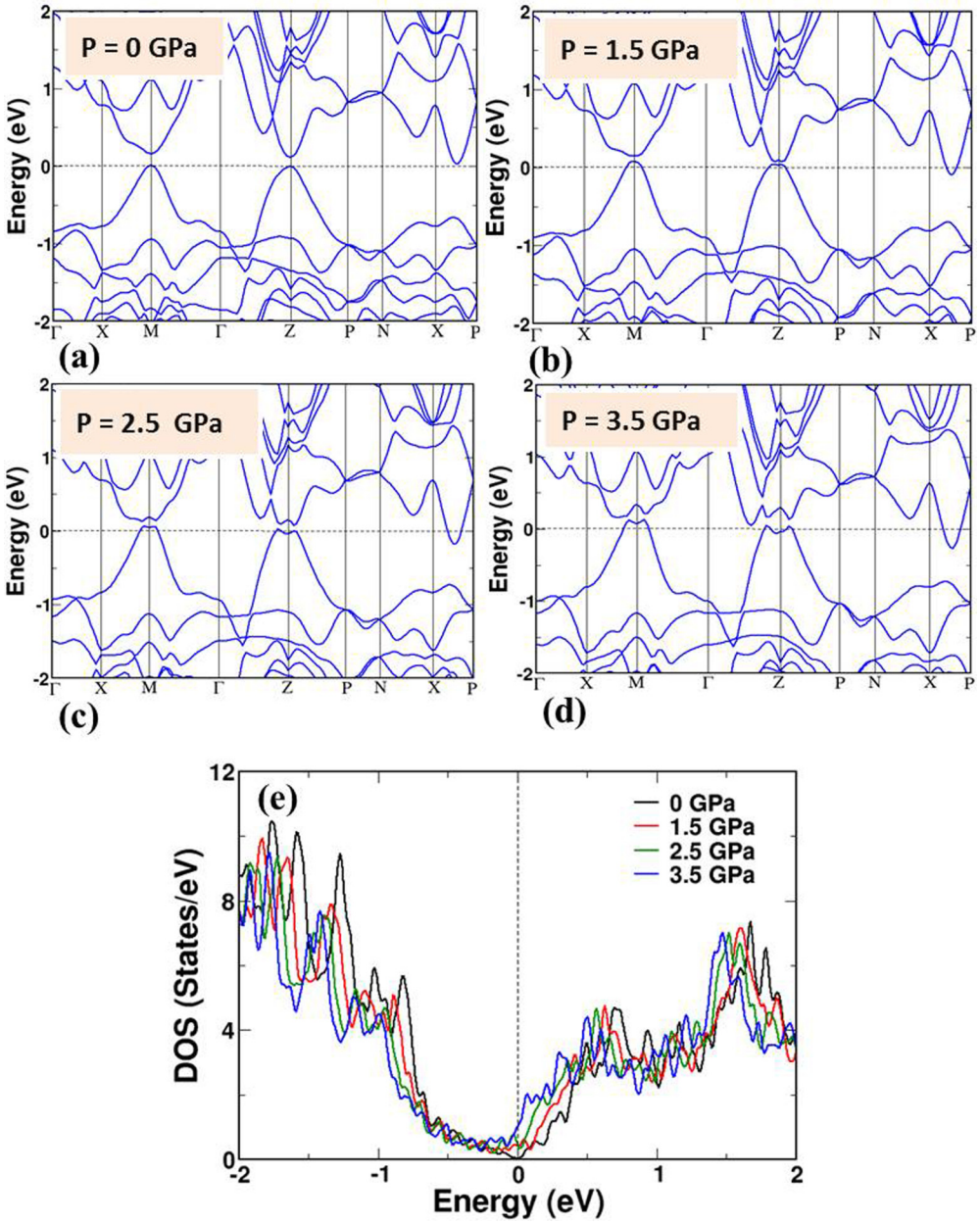

FIG. 9. (a)–(d) Electronic structure and (e) electronic density of states of InTe are calculated with spin-orbit coupling at different hydrostatic pressures. Band inversion takes place at the Z and M points in the Brillouin zone as a function of pressure near $P_C^Z = 1$ GPa and $P_C^M = 1.4$ GPa, respectively. After the band inversion, the topmost valence band and the bottom conduction band begin to cross the Fermi energy and thereby induce an onset of a semiconductor-to-metal transition in InTe.

of Fig. 8(b)]. The origin of the concave (DFT calculations) vs convex (experiment) nature of the c/a curve as a function of pressure [see inset of Fig. 8(b)] can be traced to the pressure dependence of lattice constant a. As the DFT-GGA errors in a and c are slightly different, their calculated response to pressure also has errors. The pressure dependence of the calculated lattice constant a is weaker (convex) than that of the measured one [see Fig. 8(a)]. As a result, the calculated c/a ratio exhibits a concave dependence, whereas the experimental c/a ratio shows a convex dependence with the applied pressure, though the difference between them is small.

The electronic structure of InTe calculated with inclusion of the spin-orbit interaction in the Hamiltonian reveals an indirect band gap of 0.04 eV at the optimized lattice constants, which is close to its experimental value [53] of 0.03 eV. The electronic structure of InTe exhibits valleys at the M and Z points at the boundary of the Brillouin zone with similar energies. The VBM at the M valley has slightly higher energy than the VBM at the Z valley [see Fig. 9(a)], whereas the CBM at the Z valley is slightly lower in energy than the CBM at the M valley. With increasing hydrostatic pressure, CBM and VBM in both the valleys come closer to each other and cross, resulting in

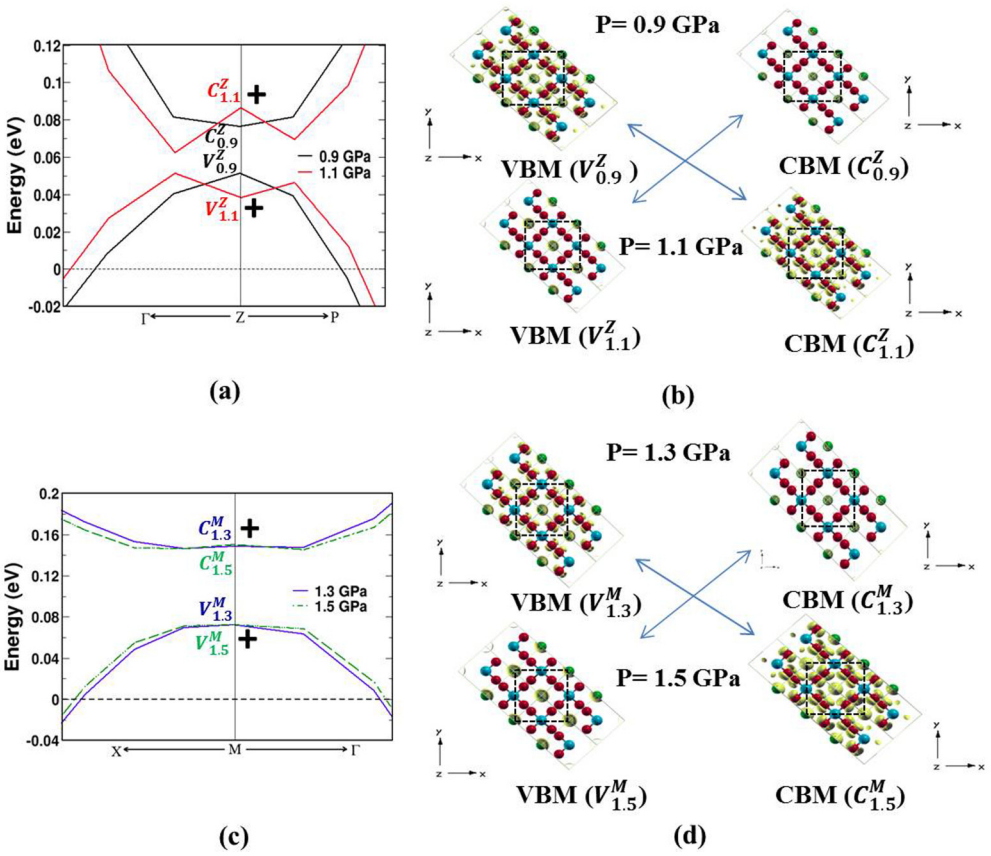

FIG. 10. Electronic structures of InTe around the (a) Z and (c) M points showing the band inversion between the top valence and lowest conduction bands as a function of hydrostatic pressures. The positive signs marked at VBM and CBM denote their parity at the Z and M points. As both of the bands have the same parity, band inversion does not change the bulk electronic topology of InTe. Isosurfaces of charge densities (b),(d) associated with valence and conduction bands (before and after the band inversion) at the Z point ($V^Z_{0.9}$, $V^Z_{1.1}$, $C^Z_{0.9}$, $C^Z_{1.1}$) and the M point ($V^M_{1.3}$, $V^M_{1.5}$, $C^M_{1.3}$, $C^M_{1.5}$) reveal that the band inversion at Z takes place in between 0.9 and 1.1 GPa (i.e., $0.9 < P^Z_C < 1.1$ GPa, hence $P^Z_C \sim 1$ GPa), whereas the band inversion at the M point occurs in between 1.3 and 1.5 GPa (i.e., $1.3 < P^M_C < 1.5$ GPa, $P^M_C \sim 1.4$ GPa). The black dashed box indicates the conventional tetragonal unit cell of InTe.

inversion of CBM and VBM at the M and Z points in the electronic structure of InTe. Band inversions in InTe take place near the pressure region $P_c = 1.0 - 1.4$ GPa. Particularly, our calculations reveal that the critical pressures (P^M_C and P^Z_C) of band inversions at the M and Z points are different. This is due to the fact that the band gaps separating the VBM and CBM at the M and Z points are different [see Figs. 10(a) and 10(c)]. At the Z point, the band inversion occurs in between 0.9 and 1.1 GPa (i.e., $0.9 < P^Z_C < 1.1$ GPa, hence $P^Z_C \sim 1$ GPa), which is evident in the isosurfaces of charge densities [see Fig. 10(b)] associated with VBM (denoted with V, i.e., $V^Z_{0.9}$, $V^Z_{1.1}$) and CBM (denoted with C, i.e., $C^Z_{0.9}$, $C^Z_{1.1}$) at 0.9 and 1.1 GPa. On the other hand, the band gap separating the VBM and CBM at the M point [see Fig. 10(c)] is slightly higher than the gap between them at the Z point [see Fig. 10(a)]. Hence, higher pressure is required to induce the band inversion at the M point. Looking at the isosurfaces of charge densities associated with VBM ($V^M_{1.3}$, $V^M_{1.5}$) and CBM ($C^M_{1.3}$, $C^M_{1.5}$) at the M point [see Fig. 10(d)] at 1.3 and 1.5 GPa, it is clear that band inversion at the M point occurs in between 1.3 and 1.5 GPa (i.e., $1.3 < P^M_C < 1.5$ GPa, hence $P^M_C \sim 1.4$ GPa). As the Fermi level [marked with the dashed horizontal line in Figs. 10(a) and 10(c)] crosses the top valence band around the M and Z points in the Brillouin zone before the critical pressures of band inversions, the system no longer remains semiconducting; rather, it becomes semimetallic [see the DOS at $P = 1.5$ GPa in Fig. 9(e)].

Figures 10(a)–10(d) shows the band inversions at the Z and M points and their associated isosurfaces of charge densities before and after the critical pressures of band inversions. Band inversion in InTe gives rise to "M" and "W"-shaped double-well features in the top of the valence and bottom of the conduction bands at the M and Z points in the Brillouin zone [e.g., see Fig. 10(a)], which are typical signatures of an inverted band structure [19]. In InTe, although band gaps at M and Z remain finite after band inversion, electronic bands close to these points and along other directions (e.g., X-P) cross the Fermi level, making InTe an ordinary semimetal. This semiconductor-to-semimetal transition is concomitant with the band inversions at the Z ($P^Z_C = 1$ GPa) and M ($P^M_C = 1.4$ GPa) points.

V. DISCUSSIONS

The band inversion is the typical indicator of the topological quantum phase transition (TQPT) in material [6,48,54]; this motivated us to check the bulk electronic topology of InTe as a

function of pressure. Symmetry analysis shows that the parity of the electronic wave functions for VBM and CBM at the M and Z points is even. Hence, we expect the band inversion not to change the topology of the bulk electronic structure. To confirm this symmetry-based argument, we determined the $\mathbb{Z}_2$ topological index using a robust and more accurate method as implemented in the Z2PACK code [42]. The calculated $\mathbb{Z}_2$ topological invariant (υ_0) of InTe remains zero before and after the band inversion, confirming no change in the electronic topology, and establishing the trivial band topology of InTe that remains unchanged through $P = P_C^Z$ and $P = P_C^M$. Although the onset of a metallic state in InTe begins with band inversion near $P \sim 1$ GPa, the complete metallization occurs only at $P \geqslant 3.5$ GPa, where both valence and conduction bands cross the Fermi level along several directions in the Brillouin zone, and DOS increases significantly across the Fermi level [see the DOS at $P = 3.5$ GPa in Fig. 9(e)]. The DOS above the Fermi level at ∼3.5 GPa are mostly contributed by $5s$ orbitals of In^{3+} and $5p$ orbital of In^{1+} ions. These band inversions ($P_C^Z = 1$ GPa and $P_C^M = 1.4$ GPa) and the complete metallization ($P = 3.5$ GPa) occur well below the critical pressure (∼ 6 GPa) of the structural phase transition ($B37$ to $B1$ structure).

Experimentally, we do not find any anomalies (within the experimental resolution) associated with a beginning of the predicted band inversion around $\sim 1.0 - 1.4$ GPa. This band inversion causes a small change in the electronic band structure, whereas the subsequent metallization introduces drastic change in it. In principle, a long-wavelength optical phonon linewidth can measure the band inversion via the electron-phonon coupling mechanism and has been reported for many compounds [4,6,18,48]. Generally, the Raman linewidth has the significant contribution from electron-phonon interactions and anharmonic phonon-phonon interactions. The phonon-phonon coupling is independent of an electronic carrier density, and hence it does not contain any information about the band inversion. In our case, as seen from Fig. 4(a), the quadratic nature of the A_{1g} mode [i.e., the nonlinear (second order) pressure coefficient of the A_{1g} mode] as a function of pressure up to ∼3.6 GPa indicates strong anharmonic phonon-phonon coupling existing in the system. Further, recently calculated [23] phonon dispersion of the InTe at the experimental lattice constants revealed an almost flat negative-frequency branch along the Γ-X-M-Γ direction in the Brillouin zone, which also supports the existence of strong anharmonic phonon-phonon interactions in InTe. The negative-frequency modes [the phonon frequency value from the calculated phonon dispersion curve is negative (i.e., imaginary)] in InTe mainly involves displacement of In^{+1} cations along the z direction, which was shown to scatter a heat-carrying acoustic phonon through anharmonic phonon-phonon interactions, and thereby giving rise to ultralow lattice thermal conductivity of InTe [23]. Hence, the presence of strong anharmonic phonon-phonon interactions at low-pressure ranges may be limiting the detection of the small electronic change (electron-phonon coupling) caused by band inversion at $\sim 1.0 - 1.4$ GPa [18]. Further, this work may be the typical example where strong phonon-phonon coupling presents; it is quite difficult to use Raman linewidth as an indirect signature for detecting the band inversion.

Upon complete metallization, the interaction between electrons and phonons is initiated, and the strength of electron-phonon coupling is expected to increase, which probably causes the sudden jump in the FWHM of the A_{1g} and E_g modes seen in our experiment near $P = 3.6$ GPa [see Figs. 4(c) and 4(d)]. Although the phonon-phonon interaction is significant in InTe (at ambient conditions) due to the presence of unstable phonon modes, the renormalization of phonon frequencies is relatively weak; hence the change in FWHM of observed Raman active modes is mainly due to electron-phonon interaction. There are several observations of a decreasing trend in the intensity of a first-order Raman mode under pressure [55,56]. However, here we have clearly observed a sudden change in the decreasing trend of the phonon modes' (A_{1g} and E_g) intensity [see Figs. 4(e) and 4(f)] at ∼3.6 GPa, which may be caused by electronic changes in InTe. The calculated DOS of InTe at around 3.5 GPa reveals metallization and we have observed anomalies in the frequency and linewidth of both modes (A_{1g} and E_g) around this pressure. Metallization due to the increased DOS increases the number of conduction electrons which would screen the incident electromagnetic light. Consequently, this will effect the Raman scattering cross section in the case of InTe. It could be one of the plausible reasons for the sudden decrease in the inelastically scattered light (Raman) intensity in InTe at high-pressure metallic regions. Earlier transport measurements showed that the coexistence of the structural transition ($B37$ to $B1$) and semiconductor-to-metal transition is due to the complete transformation of In^{3+} and In^{1+} to In^{2+} [26]. Here, our results suggest that the metallization occurs in the tetragonal phase ($B37$) itself at ∼3.6 GPa and this may act as a precursor for the structural transition to cubic phase ($B1$) at $P \sim 6$ GPa. Mention must be made that this type of pressure induced metallization without changing the oxidation state of Tl (Tl^{1+} and Tl^{3+}) was observed in the prototype compound TlSe ($B37$ phase) at ∼2.7 GPa [57]. We have analyzed the pressure-dependent Raman modes using first-principles calculations and commented on it in the Supplemental Material [47].

In the InTe compound, the same parity (+) was observed in both the VBM (mostly contributed by $5p$ orbitals of Te^{2-}) and CBM (mostly contributed by $5p$ orbitals of In^{1+}). In fact, this is a major constraint for the TQPT in InTe. So, tuning of the orbital contributions through suitable doping or substitution in either one of the parity may lead to the possibility of TQPT in this InTe. For instance, chemical substitutions induced TQPT was observed in $TlBi(S_{1-x}Se_x)_2$ [58], $Pb_{1-x}Sn_xSe$ [59], and $Bi_{1-x}Sb_x$ [60] systems without any structural transformations. Hence, we hope our result will motivate researchers to look for the possibility of modulating the parity change in InTe by altering its chemical identity (orbital characters) through suitable doping or substitution to get the nontrivial topological phase in this material. Since an even number of band inversions in a crystal with mirror symmetry generally gives rise to the topological crystalline insulating (TCI) phase (e.g., in SnTe [61] or PbTe [62]), here the possibility of having the TCI phase is not completely ruled out. So, we speculate that this kind of band inversion will lead to a significant amount of further research and detailed studies of possible topological phase transitions in InTe. Also, due to its metallization properties at a relatively low-pressure range, InTe can be used as pressure-conducting switches and pressure sensors.

VI. CONCLUSIONS

In summary, we have explored the lattice dynamical properties of InTe under hydrostatic compression up to ∼19 GPa. Our Raman spectroscopic experiment reveals pressure induced structural transitions ($B37 \rightarrow B1 \rightarrow B2$) in InTe, which shows agreement with the earlier XRD experiments. Further, an isostructural electronic transition is seen from the anomalies in the FWHM of phonon modes (E_g and A_{1g}) at a relatively low pressure around 3.6 GPa. DFT calculations show that the observed anomalies are associated with a pressure induced metallization near 3.6 GPa. The pressure coefficient of the A_{1g} and E_g modes is well correlated with the variation in lattice parameters a and c under pressure. Though InTe exhibits band inversion as a function of hydrostatic pressure, there is no change in its electronic topology ($\mathbb{Z}_2 = 0$) since it retains the same parity. Tuning of the parity with obtained band inversions in InTe may be achieved either via doping or substitutions that can open the door to considerable development of the topological phase transitions in this system.

ACKNOWLEDGMENTS

The authors gratefully acknowledge the Elettra for beamtime allotment and thank the Department of Science and Technology (DST), India for financial support. S.C.P. and C.N. acknowledge DST-SERB for the financial support under Grant No. SB/S2/CMP-019/2014. C.N. would like to acknowledge the Sheikh Saqr senior fellowship for financial support. B.J. thanks IISc Bangalore and ICTP Trieste for financial support through the award of the IISc-ICTP fellowship. K.P. thanks JNCASR for financial support through an AOARD grant from U.V.W. U.V.W. acknowledges DST for financial support through a JC Bose National fellowship.

[1] M. S. Bahramy, B. J. Yang, R. Arita, and N. Nagaosa, Nat. Commun. **3**, 679 (2012).
[2] Z. Zhao, H. Zhang, H. Yuan, S. Wang, Y. Lin, Q. Zeng, G. Xu, Z. Liu, G. K. Solanki, K. D. Patel, Y. Cui, H. Y. Hwang, and W. L. Mao, Nat. Commun. **6**, 7312 (2015).
[3] A. P. Nayak, S. Bhattacharyya, J. Zhu, J. Liu, X. Wu, T. Pandey, C. Jin, A. K. Singh, D. Akinwande, and J. F. Lin, Nat. Commun. **5**, 3731 (2014).
[4] V. Rajaji, U. Dutta, P. C. Sreeparvathy, S. C. Sarma, Y. A. Sorb, B. Joseph, S. Sahoo, S. C. Peter, V. Kanchana, and C. Narayana, Phys. Rev. B **97**, 085107 (2018).
[5] R. F. Frindt, R. B. Murray, G. D. Pitt, and A. D. Yoffe, J. Phys. C **5**, L154 (1972).
[6] A. Bera, K. Pal, D. V. S. Muthu, S. Sen, P. Guptasarma, U. V. Waghmare, and A. K. Sood, Phys. Rev. Lett. **110**, 107401 (2013).
[7] O. Gomis, R. Vilaplana, F. J. Manjón, P. Rodríguez-Hernández, E. Pérez-González, A. Muñoz, V. Kucek, and C. Drasar, Phys. Rev. B **84**, 174305 (2011).
[8] R. Vilaplana, O. Gomis, F. J. Manjón, A. Segura, E. Pérez-González, P. Rodríguez-Hernández, A. Muñoz, J. González, V. Marín-Borrás, V. Muñoz-Sanjosé, C. Drasar, and V. Kucek, Phys. Rev. B **84**, 104112 (2011).
[9] R. Vilaplana, D. Santamaría-Pérez, O. Gomis, F. J. Manjón, J. González, A. Segura, A. Muñoz, P. Rodríguez-Hernández, E. Pérez-González, V. Marín-Borrás, V. Muñoz- Sanjose, C. Drasar, and V. Kucek, Phys. Rev. B **84**, 184110 (2011).
[10] Y. A. Sorb, V. Rajaji, P. S. Malavi, U. Subbarao, P. Halappa, S. C. Peter, S. Karmakar, and C. Narayana, J. Phys.: Condens. Matter **28**, 015602 (2016).
[11] W. Feng, W. Zhu, H. H. Weitering, G. M. Stocks, Y. Yao, and D. Xiao, Phys. Rev. B **85**, 195114 (2012).
[12] Y. Ma, Y. Dai, L. Yu, C. Niu, and B. Huang, New J. Phys. **15**, 073008 (2013).
[13] C. Niu, P. M. Buhl, G. Bihlmayer, D. Wortmann, S. Blügel, and Y. Mokrousov, Nano Lett. **15**, 6071 (2015).
[14] M. Z. Hassan and C. L. Kane, Rev. Mod. Phys. **82**, 3045 (2010).
[15] L. Fu, C. L. Kane, and E. J. Mele, Phys. Rev. Lett. **98**, 106803 (2007).
[16] X. Xi, C. Ma, Z. Liu, Z. Chen, W. Ku, H. Berger, C. Martin, D. B. Tanner, and G. L. Carr, Phys. Rev. Lett. **111**, 155701 (2013).
[17] A. Ohmura, Y. Higuchi, T. Ochiai, M. Kanou, F. Ishikawa, S. Nakano, A. Nakayama, Y. Yamada, and T. Sasagawa, Phys. Rev. B **95**, 125203 (2017).
[18] K. Saha, K. Légaré, and I. Garate, Phys. Rev. Lett. **115**, 176405 (2015).
[19] K. Pal, S. Anand, and U. V. Waghmare, J. Mater. Chem. C **3**, 12130 (2015).
[20] M. Z. Torres, J. L. Pena, Y. P. Mascarenhas, R. C. Rodríguez, M. M. Lira, and O. Calzadilla, Superfic. Vacio **13**, 69 (2001).
[21] J. J. Wang, F. F. Cao, L. Jiang, Y. G. Guo, W. P. Hu, and L. J. Wan, J. Am. Chem. Soc. **131**, 15602 (2009).
[22] T. Chattopadhyay, R. P. Santandrea, and H. G. Von Schnering, J. Phys. Chem. Solids **46**, 351 (1985).
[23] M. K. Jana, K. Pal, U. V. Waghmare, and K. Biswas, Angew. Chem., Int. Ed. **55**, 7792 (2016).
[24] T. Chattopadhyay, R. P. Santandrea, and H. G. Von Schnering, Physica **139**, 353 (1986).
[25] M. K. Jacobsen, Y. Meng, R. S. Kumar, and A. L. Cornelius, J. Phys. Chem. Solids **74**, 723 (2013).
[26] S. Pal, D. N. Bose, S. Asokan, and E. S. R. Gopal, Solid State Commun. **180**, 753 (1991).
[27] V. Rajaji, P. S. Malavi, S. S. Yamijala, Y. A. Sorb, U. Dutta, S. N. Guin, B. Joseph, S. K. Pati, S. Karmakar, K. Biswas, and C. Narayana, Appl. Phys. Lett. **109**, 171903 (2016).
[28] A. Bera, A. Singh, D. V. S. Muthu, U. V. Waghmare, and A. K. Sood, J. Phys. Condens. Matter **29**, 105403 (2017).
[29] G.V. P. Kumar and C. Narayana, Curr. Sci. **93**, 778 (2007).
[30] G. J. Piermarini, S. Block, J. D. Barnett, and R. A. Forman, J. Appl. Phys. **46**, 2774 (1975).
[31] S. Klotz, J. C. Chervin, P. Munsch, and G. L. Marchand, J. Phys. D: Appl. Phys. **42**, 075413 (2009).
[32] A. P. Hammersley, S. O. Svensson, M. Hanfland, A. N. Fitch, and D. Hausermann, High Press. Res. **14**, 235 (1996).
[33] A. Boultif and D. Lour, J. Appl. Cryst. **24**, 987 (1991).

[34] A. Boultif and D. Louër, J. Appl. Cryst. **37**, 724 (2004).
[35] J. R. Carvajal, Phys. B **192**, 55 (1993).
[36] QUANTUM ESPRESSO is a community project for high-quality quantum-simulation software, based on density functional theory, and coordinated by P. Giannozzi. See http://www.quantum-espresso.org and http://www.pwscf.org (unpublished).
[37] R. M. Martin, *Electronic Structure: Basic Theory and Practical Methods* (Cambridge University Press, Cambridge, 2004).
[38] X. Hua, X. Chen, and W. A. Goddard III, Phys. Rev. B **55**, 16103 (1997).
[39] J. P. Perdew, K. Burke, and M. Ernzerhof, Phys. Rev. Lett. **77**, 3865 (1996).
[40] A. Dal Corso, Comput. Mat. Sci. **95**, 337 (2014).
[41] S. Baroni, S. de Gironcoli, A. Dal Corso, and P. Giannozzi, Rev. Mod. Phys. **73**, 515 (2001).
[42] D. Gresch, G. Autès, O. V. Yazyev, M. Troyer, D. Vanderbilt, B. A. Bernevig, and A. A. Soluyanov, Phys. Rev. B **95**, 075146 (2017).
[43] A. A. Soluyanov, and D. Vanderbilt, Phys. Rev. B **83**, 235401 (2011).
[44] J. Bhattacharjee and U. V. Waghmare, Phys. Rev. B **71**, 045106 (2005).
[45] M. A. Nizametdinova, Phys. Status Solidi B **97**, K9 (1980).
[46] A. Bera, K. Pal, D. V. S. Muthu, U. V. Waghmare, and A. K. Sood, J. Phys.: Condens. Matter **28**, 105401 (2016).
[47] See Supplemental Material at http://link.aps.org/supplemental/10.1103/PhysRevB.97.155158 for some refined XRD patterns, literature-reported c/a ratio plot, quadratic fit of the A_{1g} phonon mode, and theoretically calculated phonon modes as a function of pressures.
[48] S. N. Gupta, A. Singh, K. Pal, B. Chakraborti, D. V. S. Muthu, U. V. Waghmare, and A. K. Sood, Phys. Rev. B **96**, 094104 (2017).
[49] I. Efthimiopoulos, J. Zhang, M. Kucway, C. Park, R. C. Ewing, and Y. Wang, Sci. Rep. **3**, 2665 (2013).
[50] A. C. Ho, R. C. Hanson, and A. Chizmeshya, Phys. Rev. B **55**, 14818 (1997).
[51] J. H. C. Hogg and H. H. Sutherland, Acta Cryst. B **32**, 2689 (1976).
[52] F. D. Murnaghan, Proc. Nat. Acad. Sci. USA **30**, 244 (1944).
[53] M. Parlak, C. Ercelebi, I. Gunal, H. Ozkan, and N. M. Gasan, Cryst. Res. Technol. **31**, 673 (1996).
[54] K. Pal and U. V. Waghmare, Appl. Phys. Lett. **105**, 062105 (2014).
[55] D. Olego and M. Cardona, Phys. Rev. B **25**, 1151 (1982).
[56] G. Lucazeau, J. Raman Spectrosc. **34**, 478 (2003).
[57] M. K. Rabinal, S. Asokan, M. O. Godazaev, N. T. Mamedov, and E. S. R. Gopal, Phys. Status Solidi B **167**, K97 (1991).
[58] S. Y. Xu, Y. Xia, L. A. Wray, S. Jia, F. Meier, J. H. Dil, J. Osterwalder, B. Slomski, A. Bansil, H. Lin, R. J. Cava, and M. Z. Hasan, Science **332**, 560 (2011).
[59] P. Dziawa, B. J. Kowalski, K. Dybko, R. Buczko, A. Szczerbakow, M. Szot, E. Łusakowska, T. Balasubramanian, B. M. Wojek, M. H. Berntsen, O. Tjernberg, and T. Story, Nat. Mater. **11**, 1023 (2012).
[60] D. Hsieh, D. Qian, L. Wray, Y. Xia, Y. Hor, R. J. Cava, and M. Z. Hasan, Nature (London) **452**, 970 (2008).
[61] T. H. Hsieh, H. Lin, J. Liu, W. Duan, A. Bansil, and L. Fu, Nat. Commun. **3**, 982 (2012).
[62] P. Barone, T. Rauch, D. Di Sante, J. Henk, I. Mertig, and S. Picozzi, Phys. Rev. B **88**, 045207 (2013).